Band instability in near-critical fluids subjected to vibration under weightlessness

T. Lyubimova,[1,2] A. Ivantsov,[1,2] Y. Garrabos,[3,4] C. Lecoutre,[3,4] G. Gandikota,[5] and D. Beysens[5,6]

[1]*Institute of Continuous Media Mechanics UB RAS, 1, Koroleva Street, 614013 Perm, Russia*

[2]*Perm State University, 15, Bukireva Street 614990 Perm, Russia*

[3]*CNRS, ICMCB, ESEME, UPR 9048, F-33600 Pessac, France*

[4]*Université Bordeaux, ICMCB, UPR 9048, F-33600 Pessac, France*

[5]*Service des Basses Températures, CEA-Grenoble and Université Joseph Fourier, F-38000 Grenoble, France*

[6]*Physique et Mécanique des Milieux Hétérogènes, UMR 7636 CNRS–ESPCI–Université Pierre et Marie Curie–Université Paris Diderot, 10 rue Vauquelin, 75005 Paris, France*

(Received 27 July 2016; revised manuscript received 6 December 2016; published 10 January 2017)

Periodical patterns (bands) developing at the interface of two immiscible fluids under vibration parallel to interface are observed under zero-gravity conditions. Fluids are slightly below their liquid-vapor critical point where they behave in a scaled, universal manner. In addition, liquid and vapor densities are close and surface tension is very low. Linear stability analyses and direct numerical simulation show that this instability, although comparable to the frozen wave instability observed in a gravity field, is nonetheless noticeably different when gravity becomes zero. In particular, the neutral curve minimum corresponds to the long-wave perturbations with $k = 0$ and zero dimensionless vibrational parameter, corresponding to no instability threshold. The pattern wavelength thus corresponds to the wavelength of the perturbations with maximal growth rate. This wavelength differs substantially from the neutral perturbations wavelength at the same vibrational parameter value. The role of viscosity is highlighted in the pattern formation, with a critical wavelength dependence on vibration parameters that strongly depends on viscosity. These results compare well with experimental observations performed in the liquid-vapor phases near the critical point of CO_2 (in weightlessness) and H_2 (under magnetic levitation).

DOI: 10.1103/PhysRevE.95.013105

I. INTRODUCTION

When subjected to vibration, the interface shape and stability depend on the relative direction of the vibration and the interface. Vibration perpendicular to the interface leads to its parametric excitation (known as the Faraday wave instability [1,2]). Vibration parallel to the fluid interface can lead to the formation of quasistationary wave patterns [3] caused by a shear-driven mechanism similar to the Kelvin-Helmholtz (KH) instability [4]. This instability was later called frozen wave instability [5] as the interface deformation is immobile in the reference frame of oscillating boundaries. The gravity acceleration g is an important factor in the formation of these instabilities.

A question arises about how these instabilities can transform when gravity is near zero, as is the case in space. To answer this question, it is interesting to use fluids near their critical point. The interesting aspect of the critical point vicinity is the possibility to vary simply by changing temperature the important parameters of the instability: liquid-vapor interfacial tension and density difference (and in a lesser amount, viscosity) in a universal, scaling way [6–8]. However, the study of these instabilities close to the critical point necessitates very fine temperature regulation and establishing zero-gravity conditions in order to remove inevitable initial density stratification and strong thermal instabilities.

The cancellation of gravity forces can be achieved by different means. We here refer to (i) sounding rockets experiments performed with a cylindrical cell filled with CO_2 near and below its critical point (critical temperature 304 K) [9–11] and (ii) magnetic compensation of gravity forces in a cubic cell filled with H_2 (critical temperature 33 K) [10,12,13]. Faraday instabilities on an interface perpendicular to vibrations have been observed and studied in H_2 under weightlessness [14].

Closer to the critical point another instability develops where the vapor-liquid interface orders in periodical bands perpendicular to the vibration direction. This phenomenon was observed in experiments conducted on CO_2 [9–11] and H_2 [10,12]. The band pattern appears only within a few mK to T_c, in a temperature range where Faraday waves do not show up anymore as a square pattern but as a line pattern [9]. Indeed, as T_c is approached, the Faraday wavelength decreases, thus involving increasing viscous dissipation that forces a pattern transition from square to line due to enhanced dissipation [9,15]. In Fig. 1 is reported such pattern observed in CO_2 and H_2. One notes that, depending on the vibration characteristics, a Faraday instability can also develop.

In a study of H_2 under various gravitational acceleration (g) of the frozen wave instability [14], it has been observed that the wave amplitude was increasing as $g^{-0.7}$ when g was decreased. It was noted that when this amplitude becomes larger than the cell height, a band pattern was observed. It can then be thought that the band pattern is the extrapolation of the frozen wave pattern when $g \to 0$. Although both instabilities have the same origin (shear flow at the interface) we will see in the next sections that its characteristics cannot be simply deduced from a mere extrapolation at $g = 0$ of the frozen wave instability. Development of band patterns in the conditions where gravity acceleration is negligible in comparison with the vibrational acceleration was predicted theoretically in [16].

It is the object of this paper to investigate theoretically and experimentally in detail the band instability that occurs in weightlessness. Section II A presents the problem formulation; Secs. II B and II C, the review of theoretical investigations for the case where viscosity is neglected; and Sec. II D, the problem formulation, the base flow analysis, and the formulation of the linear stability problem for viscous fluids.

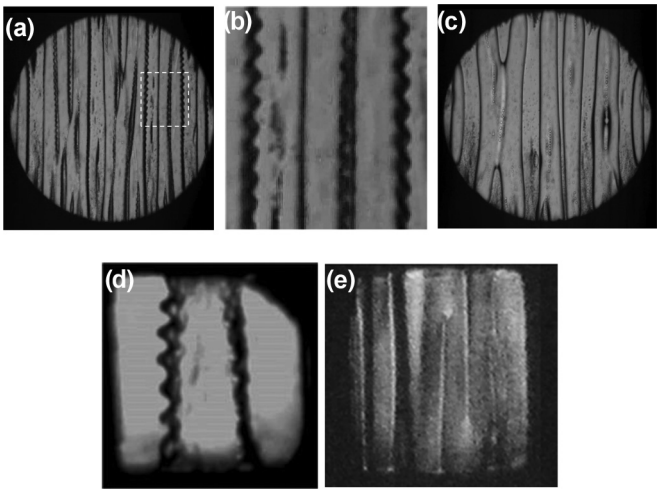

FIG. 1. Band pattern under weightlessness. (a–c) CO_2 at $T_c - 2.4$ mK, in cell with diameter 10.00 mm and thickness 2.189 mm. (a) $a = 0.7$ mm and $f = 10.37$ Hz, where a line pattern of Faraday waves are visible on the interfaces. The window is enlarged in (b). (c) $a = 0.2$ mm and $f = 25.28$ Hz, where no Faraday waves are visible. (d,e) H_2 in $3 \times 3 \times 2$ mm^3 cell. (d) $T_c - 10$ mK, $a = 0.83$ mm, and $f = 20$ Hz. Faraday waves (line pattern) are observed. (e) $T_c - 5$ mK, $a = 0.29$ mm, and $f = 40$ Hz. No Faraday waves are visible.

Results of a two-dimensional (2D) direct numerical simulation (DNS) are then reported in Sec. III, taking into account viscosity. Section IV deals with the comparison of linear stability theory with DNS. Section V is concerned with experimental results performed in H_2 and CO_2 and comparison is made with linear stability analysis. Concluding remarks are given in Sec. VI.

II. THEORETICAL BACKGROUND. WAVE NUMBER SELECTION

A. Problem formulation. Governing equations and boundary conditions

Let us consider the general case of a fluid interface in two superposed horizontal layers of immiscible incompressible viscous fluids of different densities. The fluids are subjected to a gravity field and to horizontal vibrations at angular frequency ω (frequency $f = \omega/2\pi$) and amplitude a. A Cartesian coordinate system is chosen in such a way that in the absence of vibrations the denser fluid occupies the domain $-h < z < 0$ and the less dense fluid, the domain $0 < z < h$ (for sake of simplicity the layers are assumed to have the same thickness). In the absence of vibrations the interface is flat and horizontal and its position corresponds to the plane $z = 0$. The governing equations describing the behavior of this system in the reference frame of oscillating layer boundaries are

$$\frac{\partial \vec{v}_\beta}{\partial t} + (\vec{v}_\beta \vec{\nabla})\vec{v}_\beta = -\frac{1}{\rho_\beta}\vec{\nabla} p_\beta + \nu_\beta \Delta \vec{v}_\beta - g\vec{\gamma} + a\omega^2 \cos \omega t \, \vec{j}, \quad \operatorname{div} \vec{v}_\beta = 0. \tag{1}$$

The subscript β refers to the fluids: $\beta = 1$ corresponds to the lower and denser fluid and $\beta = 2$ to the upper and lighter fluid; $\vec{v}_\beta$, p_β are the velocity and pressure in the βth fluid; g is the gravity acceleration value; $\vec{\gamma}$ is the unit vector in vertical direction; $\vec{j}$ is the unit vector in the direction of vibrations; ρ_β, ν_β are the density and kinematic viscosity of the βth fluid.

The boundary conditions on the external rigid boundaries are the no-slip conditions:

$$z = -h: \ \vec{v}_1 = 0; \quad z = h: \ \vec{v}_2 = 0. \tag{2}$$

The boundary conditions on the fluid interface described by the equation $z = \zeta(x,y,t)$ are the velocity continuity, the kinematic condition, and the stress balance conditions:

$$\vec{v}_1 = \vec{v}_2, \quad \frac{\partial \zeta}{\partial t} + \vec{v}_1 \cdot \vec{\nabla}\zeta = \vec{v}_1 \cdot \vec{\gamma},$$
$$[p]n_i = [T_{ij}]n_j + \alpha n_i \operatorname{div} \vec{n}. \tag{3}$$

Here α is the interfacial tension between the fluids, $\vec{n}$ is the unit vector normal to the interface, T_{ij} is the viscous stress tensor, and square brackets denote the jump of quantity across the interface $[f] = f_1 - f_2$.

We study the behavior of a two-layer system in the configuration close to the experimental configuration where the container with rigid boundaries is of large but finite length. To model this situation the integral flow closeness (or total volume conservation) condition is imposed:

$$\int_{-h}^{\zeta} \vec{v}_1 \cdot \vec{j} \, dz + \int_{\zeta}^{h} \vec{v}_2 \cdot \vec{j} \, dz = 0. \tag{4}$$

B. Formation of frozen waves

In the experiments [3] concerning two liquid layers under earth gravity field, it was found that at some values of the vibration parameters, a quasistationary wave pattern (frozen waves) forms at the interface. A theoretical description of the frozen wave formation in a two-layer system of fluids under earth gravity was originally suggested in [4], where a theoretical approach describing the dynamics of fluid interfaces under high-frequency and small-amplitude vibrations was developed. In this theory all hydrodynamic fields are decomposed into pulsation (quickly oscillating) and average (slowly varying) components and the closed system of equations for average and pulsation fields is obtained by multiple scale method:

$$\frac{\partial \vec{u}_\beta}{\partial t} + (\vec{u}_\beta \vec{\nabla})\vec{u}_\beta = -\vec{\nabla}\left(\frac{p_\beta}{\rho_\beta} + \frac{a^2\omega^2 V_\beta^2}{4}\right) + \nu_\beta \Delta \vec{u}_\beta - g\vec{\gamma},$$
$$\operatorname{div} \vec{u}_\beta = 0, \tag{5}$$

$$\operatorname{curl} \vec{W}_\beta = 0, \quad \operatorname{div} \vec{W}_\beta = 0. \tag{6}$$

Here $\vec{u}_\beta$, p_β are the average velocity and pressure; $\vec{V}_\beta$ is the pulsation velocity amplitude in the reference frame of oscillating layers; $\vec{W}_\beta$ is the pulsation velocity amplitude in the laboratory reference frame related to $\vec{V}_\beta$ as $\vec{W}_\beta = \vec{V}_\beta + \vec{j}$.

Equations (6) for pulsations do not contain the viscous and nonlinear terms. It was possible to neglect these terms due to the assumptions of high frequency (and therefore small thickness of the viscous boundary layer) and small amplitude of the vibrations.

At the rigid boundaries the no-slip condition for average velocity and impermeability condition for pulsation velocity are imposed:

$$\vec{u}_\beta = 0, \quad W_{\beta n} = 0. \tag{7}$$

The conditions at the fluid interface are the continuity conditions for the pulsation pressure, normal component (normal is indicated by the subscript n) of pulsation velocity and average velocity, the kinematic condition, and the stress balance condition:

$$\begin{gathered}\rho_1 W_{1\tau} = \rho_2 W_{2\tau}, \quad W_{1n} = W_{2n}, \\ \vec{u}_1 = \vec{u}_2, \quad \frac{\partial \zeta}{\partial t} + \vec{u}_1 \cdot \vec{\nabla}\zeta = \vec{u}_1 \cdot \vec{\gamma}, \\ \frac{a^2\omega^2}{2} V_n[\rho W_i] = -[p]n_i + [T_{ij}]n_j + \alpha(\operatorname{div}\vec{n})n_i\end{gathered} \tag{8}$$

Here T_{ij} is the viscous stress tensor defined with the average velocity field and the subscript τ stands for the tangential components.

Based on the theoretical model Eqs. (5)–(8), Ref. [4] considered the development of frozen waves in a system of two superposed horizontal layers of immiscible incompressible fluids subjected to gravity field and horizontal high-frequency small-amplitude vibrations. For sake of simplicity the viscosity was neglected in the description of average fields, i.e., in the momentum equation and in the stress balance condition. The fully inviscid problem was thus considered:

$$\frac{\partial \vec{u}_\beta}{\partial t} + (\vec{u}_\beta \vec{\nabla})\vec{u}_\beta = -\vec{\nabla}\left(\frac{p_\beta}{\rho_\beta} + \frac{a^2\omega^2 V_\beta{}^2}{4}\right) - g\vec{\gamma},$$

$$\operatorname{div}\vec{u}_\beta = 0, \tag{9}$$

$$\operatorname{curl}\vec{W}_\beta = 0, \quad \operatorname{div}\vec{W}_\beta = 0, \tag{10}$$

$$z = -h: \quad \vec{u}_1 = 0, \quad W_{1\,n} = 0, \quad z = h: \quad \vec{u}_2 = 0, \quad W_{2n} = 0, \tag{11}$$

$$\begin{gathered}z = \zeta: \quad \rho_1 W_{1\tau} = \rho_2 W_{2\tau}, \quad W_{1n} = W_{2n}, \\ \vec{u}_1 = \vec{u}_2, \quad \frac{\partial \zeta}{\partial t} + \vec{u}_1 \cdot \vec{\nabla}\zeta = \vec{u}_1 \cdot \vec{\gamma}, \\ \frac{a^2\omega^2}{2} V_n[\rho W_i] = -[p]n_i + \alpha(\operatorname{div}\vec{n})n_i.\end{gathered} \tag{12}$$

In the framework of this approach a complete analytical solution of the problem Eqs. (9)–(12) was obtained in [4]. It was shown that the problem Eqs. (9)–(12) gives a solution which corresponds to the quasiequilibrium state where the interface is planar, the average flow is absent ($\vec{u}_\beta = 0$), and the pulsation flow represents time-periodic parallel flows with different velocity amplitudes in two fluids satisfying the pulsation flow closeness conditions (under inviscid approximation the amplitudes of the pulsation velocities in two fluids do not depend on the coordinates):

$$\zeta = 0, \quad \vec{W}_1 = \left(\frac{2}{\rho+1}, 0, 0\right),$$

$$\vec{W}_2 = \left(\frac{2\rho}{\rho+1}, 0, 0\right),$$

$$\vec{V}_1 = \left(\frac{1-\rho}{\rho+1}, 0, 0\right),$$

$$\vec{V}_2 = \left(\frac{\rho-1}{\rho+1}, 0, 0\right),$$

$$\int_{-h}^{0} V_{1x}\,dz + \int_{0}^{h} V_{2x}\,dz = 0. \tag{13}$$

Here $\rho = \rho_1/\rho_2$ is the density ratio.

By analyzing the linear stability of the quasiequilibrium state Eq. (13) an explicit formula for the neutral curve was obtained [4]:

$$(a\omega)^2 = \frac{(\rho_1+\rho_2)^3}{2\rho_1\rho_2(\rho_1-\rho_2)^2}\left[\alpha k^* + (\rho_1-\rho_2)\frac{g}{k^*}\right]\tanh(k^*h). \tag{14}$$

Here $k^* = 2\pi/\lambda^*$ is the wave number of instability with wavelength λ^*.

Similarly to the case of the KH instability at the interface of two stationary parallel flows, it follows from the above Eq. (14) that the long-wave perturbations are responsible for a stability loss under zero-gravity conditions (see the terms inside the brackets). Moreover, under such weightless conditions the stabilizing effect of gravity is not present any more and there is no instability threshold. The neutral curve (14) does not show a minimum, i.e. the instability can develop at any small values of the vibrational velocity amplitude ($a\omega$). As a consequence, the question of wavelength selection does arise under zero-gravity conditions.

C. Wavelength selection under zero gravity. Inviscid case

One hypothesis on the wavelength selection was suggested in [17] where it was assumed that the wavelength selection in this problem was related to the growth rate of perturbations: The pattern with the wavelength that corresponds to the perturbations with maximal growth rate is realized. In [17] this hypothesis was implemented for the calculation of the wavelength of periodical patterns arising at the interface of two incompressible inviscid fluids subjected to tangential vibrations under zero-gravity conditions, i.e., for the problem Eqs. (9)–(12) with $g = 0$.

For two-dimensional perturbations of the base state [Eq. (13)] not depending on the y coordinate and having zero y-velocity components, it is convenient to introduce stream functions for the perturbations of average and pulsation components of the velocities:

$$u_{1x} = \frac{\partial \psi_1}{\partial z}, \quad u_{1z} = -\frac{\partial \psi_1}{\partial x}, \quad u_{2x} = \frac{\partial \psi_2}{\partial z}, \quad u_{2z} = -\frac{\partial \psi_2}{\partial x}. \tag{15}$$

In terms of stream function the pulsation velocities of two fluids in the base state are written as

$$\begin{gathered}W_{1x} = \frac{2}{\rho+1} + \frac{\partial \Psi_1}{\partial z}, \quad W_{1z} = -\frac{\partial \Psi_1}{\partial x}, \\ W_{2x} = \frac{2\rho}{\rho+1} + \frac{\partial \Psi_2}{\partial z}, \quad W_{2z} = -\frac{\partial \Psi_2}{\partial x},\end{gathered} \tag{16}$$

and the dimensionless equations and boundary conditions for

small perturbations of this base state have the form

$$\frac{\partial}{\partial t}\frac{\partial \psi_1}{\partial z} = \frac{1-\rho}{\rho}\frac{\partial p_1}{\partial x}, \quad -\frac{\partial}{\partial t}\frac{\partial \psi_1}{\partial x} = \frac{1-\rho}{\rho}\frac{\partial p_1}{\partial z},$$
$$\frac{\partial}{\partial t}\frac{\partial \psi_2}{\partial z} = (1-\rho)\frac{\partial p_2}{\partial x}, \quad -\frac{\partial}{\partial t}\frac{\partial \psi_2}{\partial x} = (1-\rho)\frac{\partial p_2}{\partial z}, \tag{17}$$

$$\Delta\psi_j = 0, \ \ \Delta\Psi_j = 0, \tag{18}$$

$$z = -1: \ \ \frac{\partial \psi_1}{\partial x} = 0, \ \ \Psi_1 = 0, \tag{19}$$

$$z = 1: \ \ \frac{\partial \psi_2}{\partial x}, \ \ = 0\Psi_2 = 0, \tag{20}$$

$$z = 0: \ \ \frac{\partial \psi_1}{\partial x} = \frac{\partial \psi_2}{\partial x}, \ \ \rho\frac{\partial \Psi_1}{\partial z} = \frac{\partial \Psi_2}{\partial z},$$
$$\Psi_1 - \Psi_2 = 2\frac{\rho-1}{\rho+1}\zeta, \tag{21}$$

$$\frac{\partial \zeta}{\partial t} = -\frac{\partial \psi_1}{\partial x}, \ \ \pi_1 - \pi_2 + \frac{4B}{\rho+1}\frac{\partial \Psi_2}{\partial z} + \frac{\partial^2 \zeta}{\partial x^2} = 0.$$

Here

$$B = \frac{(a\omega)^2 h(\rho_1-\rho_2)}{4\alpha} \tag{22}$$

is the dimensionless vibrational parameter. Equations (17)–(21) are written in dimensionless form. The following quantities are chosen for scaling: the thickness of each layer h for length scale, $(\rho_1-\rho_2)$ for density scale, $\sqrt{(\rho_1-\rho_2)h^3/\alpha}$ for time scale, $\sqrt{\alpha/[(\rho_1-\rho_2)h]}$ for velocity scale, and α/h for pressure scale.

For normal-mode perturbations in the form $\sim \exp(ikx)\exp(\sigma t)$, Eqs. (17) and (18) are reduced to a system of ordinary differential equations (ODEs) depending only on the z coordinate with constant coefficients for the amplitudes. The substitution of the solution of this system of ODE into the boundary conditions gives a linear homogeneous system of algebraic equations for the coefficients, which leads to the expression for the exponential growth rate σ or σ^* in dimensional form. With $k = k^*h$,

$$\sigma^2 = \frac{8B\rho k^2(\rho-1)^2}{(\rho+1)^4} - \frac{\rho-1}{\rho+1}k^3\tanh(k), \tag{23}$$

or in dimensional form,

$$\sigma^{*2} = 2a^2\omega^2\frac{\rho_1\rho_2(\rho_1-\rho_2)^2}{(\rho_1+\rho_2)^4}k^{*2} - \frac{1}{(\rho_1+\rho_2)}\alpha k^{*3}\tanh(k^*h). \tag{24}$$

By setting $\sigma = 0$ one obtains the neutral curve

$$B = \frac{(\rho+1)^3}{8\rho(\rho-1)}k\tanh(k), \tag{25}$$

or in dimensional form,

$$(a\omega)^2 = \frac{(\rho_1+\rho_2)^3}{2\rho_1\rho_2(\rho_1-\rho_2)^2}\alpha k^*\tanh(k^*h), \tag{26}$$

which coincides with Eq. (14) when $g = 0$.

By calculating the coordinates of the maximum of the curve $\sigma(k)$ from Eq. (23) one obtains a relation between the dimensionless vibrational parameter and the dimensionless wave number of perturbations with maximal growth rate:

$$B = \frac{(\rho+1)^3}{16\rho(\rho-1)}\left(3k\tanh(k) + \frac{k^2}{\mathrm{ch}^2(k)}\right), \tag{27}$$

or in dimensional form,

$$(a\omega)^2 = \frac{(\rho_1+\rho_2)^3}{4\rho_1\rho_2(\rho_1-\rho_2)^2}\alpha k^*\left[3\tanh(k^*h) + \frac{k^*h}{\cosh^2(k^*h)}\right]. \tag{28}$$

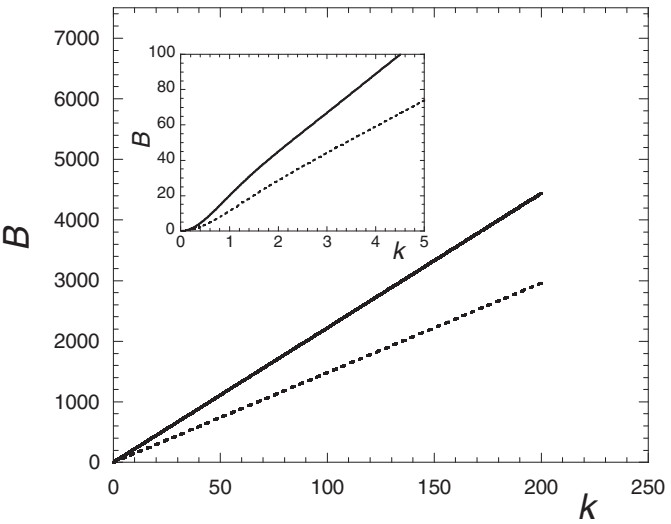

FIG. 2. Dependence of the dimensionless vibrational parameter B on the dimensionless wave number k for $\rho = 1.07$. Interrupted curve: Neutral perturbations with $\sigma = 0$ in an inviscid fluid. Full curve: Perturbations with maximal growth rate in an inviscid fluid. Inset: Small k behavior.

It is seen from (27) that for $k > 1$ the dependence of B on the wave number of the perturbations with the maximal growth rate is close to a linear law.

In Fig. 2 we plot the dependences of B on k for the neutral perturbations with $\sigma = 0$ [Eq. (14)] and for the perturbations with maximal growth rate obtained in the inviscid approximation [Eq. (27)] at $\rho = 1.07$ (this value corresponds to the parameters of space experiments discussed below in Sec. V). As one can see, for the same value of B, the wave number of perturbations with maximal growth rate is substantially smaller than the wave number of neutral perturbations. Moreover, the difference grows rapidly with the increase of B.

D. Wavelength selection under zero gravity. Viscous fluids

For viscous fluids it is not possible to obtain analytical expressions similar to (23). In this case the problem should be solved numerically by the solution of a linearized problem on the evolution of small perturbations of the base state.

The governing equations describing the fluid behavior in the reference frame of the oscillating layers are (in dimensionless form and at $g = 0$)

$$\frac{\partial \vec{v}_\beta}{\partial t} + A(\vec{v}_\beta\vec{\nabla})\vec{v}_\beta = -\frac{1}{\rho_\beta}\vec{\nabla}p_\beta + \nu_\beta\Delta\vec{v}_\beta - \vec{j}\cos t,$$
$$\mathrm{div}\,\vec{v}_\beta = 0. \tag{29}$$

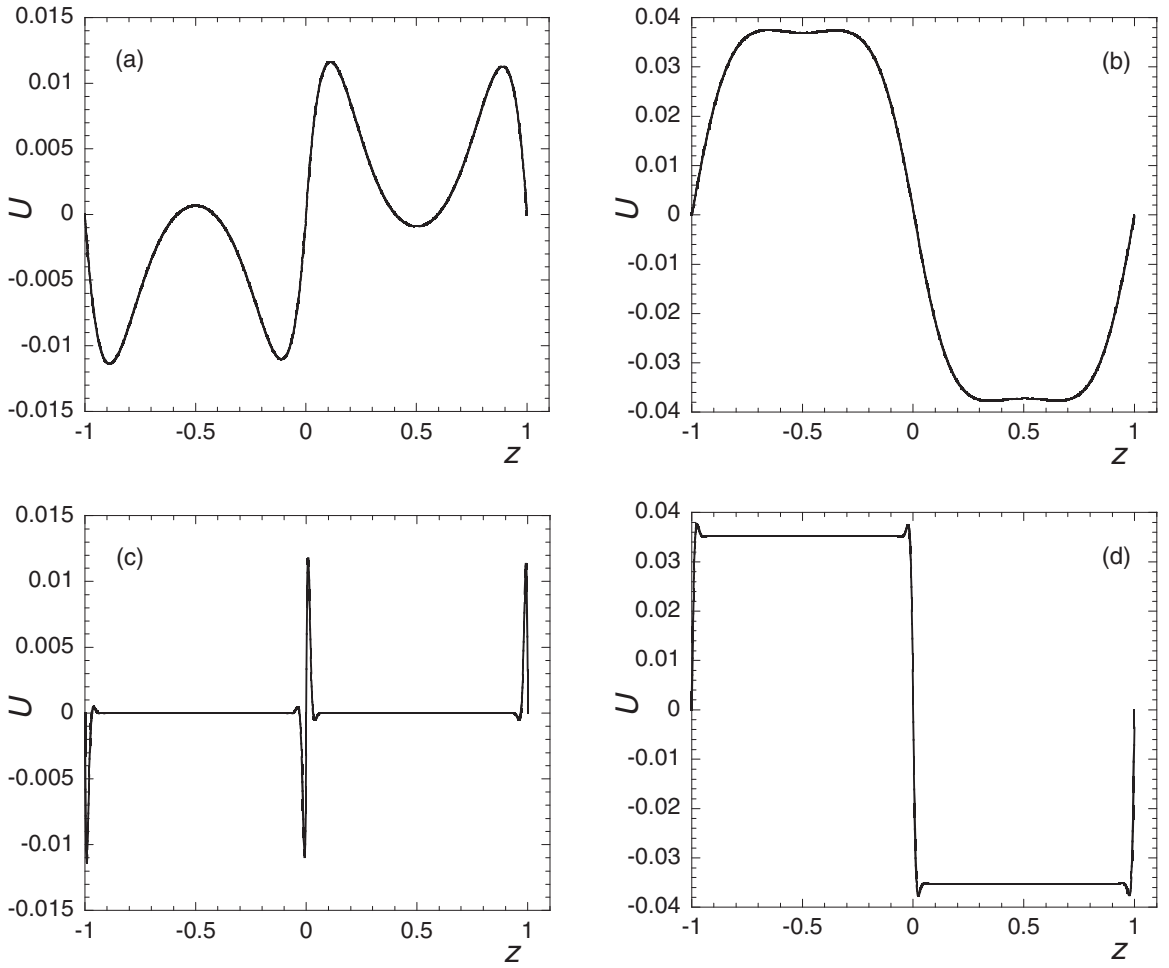

FIG. 3. Base flow velocity profiles for $\rho_1/\rho_2 = 1.07$ and two sets of dimensionless viscosities: (a,b) $\nu_1 = \nu_2 = 0.01$; (c,d) $\nu_1 = \nu_2 = 5 \times 10^{-5}$ (typical of CO_2 experiments in Sec. V). Snapshots are taken at two phases of vibration period (a,c) $\varphi = 0$ and (b,d) $\varphi = \pi/2$.

Here $\vec{v}_\beta, p_\beta$ are the dimensionless velocity and pressure, respectively, in the βth fluid; $A = a/h$ is the dimensionless amplitude of vibrations; $\rho_\beta = \rho^*_\beta/\rho^*_1$, $\nu_\beta = \nu^*_\beta/h^2\omega$ are the dimensionless density and viscosity of the βth fluid with $\rho^*_\beta, \nu^*_\beta$ the dimensional density and viscosity. The following quantities were used as scales: the thickness of each layer h for length scale, ω^{-1} for time scale, $a\omega$ for velocity scale, $\rho^*_1 ha\omega^2$ for pressure scale.

The boundary conditions on the external rigid boundaries are the no-slip conditions,

$$z = -1: \quad \vec{v}_1 = 0; \quad z = 1: \quad \vec{v}_2 = 0. \tag{30}$$

The boundary conditions on the fluid interface $z = \zeta(x,t)$ are the continuity of the velocity, the kinematic condition, and the normal stress balance conditions,

$$z = \zeta(x,t): \quad \vec{v}_1 = \vec{v}_2, \quad \frac{\partial \zeta}{\partial t} + A\mathrm{v}_{x1}\frac{\partial \zeta}{\partial x} = A\mathrm{v}_{z1}, \tag{31}$$

$$p_1 - p_2 = \sigma_{nn1} - \sigma_{nn2} - A^{-1}\,\mathrm{We}^{-1}\frac{\partial^2 \zeta}{\partial x^2}. \tag{32}$$

Here $\mathrm{We} = h^3\rho^*_1\omega^2/\alpha$ is the Weber number. The dimensionless vibrational parameter B introduced earlier is related to the parameters A and We as $B = A^2\,\mathrm{We}\,(\rho - 1)/4\rho$.

The total volume conservation condition is

$$\int_{-1}^{\zeta} \mathrm{v}_{x1}dz + \int_{\zeta}^{1} \mathrm{v}_{x2}dz = 0. \tag{33}$$

Similar to the inviscid case, the problem Eqs. (29)–(33) allows a solution with a flat interface. The only nonzero velocity component in each fluid in this base state is the horizontal component; however, now this component depends not only on time but also on the vertical coordinate: $\mathrm{v}_{x0\beta} \equiv U_\beta = U_\beta(z,t)$. The problem for this base flow was solved by using the MAPLE package for analytical calculations. Velocity profiles at two phases of the vibration period for $\rho_1/\rho_2 = 1.07$ and two sets of dimensionless viscosities are presented in Fig. 3. In the low-viscous case thin boundary layers can be observed near the rigid boundaries and near the fluid interface.

Linear stability of the base state was studied numerically by the solution of linearized equations and boundary conditions for small two-dimensional perturbations periodical in the x direction ($\sim \exp(ikx)$):

$$\frac{\partial u_\beta}{\partial t} + ikAU_\beta u_\beta + Aw_\beta\frac{\partial U_\beta}{\partial z} = -\frac{ik}{\rho_\beta}p_\beta + \nu_\beta\left(\frac{\partial^2 u_\beta}{\partial z^2} - k^2 u_\beta\right),$$

$$\frac{\partial w_\beta}{\partial t} + ikAU_\beta w_\beta = -\frac{1}{\rho_\beta}\frac{\partial p_\beta}{\partial z} + \nu_\beta\left(\frac{\partial^2 w_\beta}{\partial z^2} - k^2 w_\beta\right),$$

$$iku_\beta + \frac{\partial w_\beta}{\partial z} = 0, \tag{34}$$

$$z = -1: \quad u_1 = w_1 = 0; \quad z = 1: \quad u_2 = w_2 = 0, \tag{35}$$

$$z = 0: \quad u_1 + \frac{\partial U_1}{\partial z}\zeta = u_2 + \frac{\partial U_2}{\partial z}\zeta,$$

$$w_1 = w_2, \quad \frac{\partial \zeta}{\partial t} + ikAU_1\zeta = Aw_1,$$

$$p_1 - p_2 + 2\left(\eta_2\frac{\partial w_2}{\partial z} - \eta_1\frac{\partial w_1}{\partial z}\right) + A^{-1}\,\mathrm{We}^{-1}k^2\zeta = 0,$$

$$A\eta_1\left(\frac{\partial u_1}{\partial z} + ikw_1 + \zeta\frac{\partial^2 U_1}{\partial z^2}\right) - A\eta_2\left(\frac{\partial u_2}{\partial z} + ikw_2 + \zeta\frac{\partial^2 U_2}{\partial z^2}\right) = 0. \tag{36}$$

Here u_β and w_β are the x and z components of the velocity perturbations in the βth fluid, p_β is the pressure perturbation, k is the wave number, and $\eta_\beta = \nu_\beta\rho_\beta$ is the dynamic viscosity.

Numerical solutions of the problem Eqs. (34)–(36) was carried out by the finite difference method. The perturbation growth rate was calculated by using numerical data on the perturbation field variation during a period of vibrations. The results are discussed in Secs. III–V where they are compared to the results of a direct numerical simulation (Sec. IV) and experiment (Sec. V).

III. DIRECT NUMERICAL SIMULATIONS

To verify the applicability of the assumption that the pattern with the wavelength corresponding to the perturbations with maximal growth rate is realized we performed direct numerical simulation (DNS) of the pattern formation on the interface for a system of incompressible viscous fluids. The simulation was carried out in the framework of a two-dimensional approach for a two-layer system of immiscible incompressible viscous fluids filling a rectangular container with horizontal size much larger than the vertical size.

The modeling is carried out using the volume of fluid (VoF) method describing the dynamics of the interface of immiscible fluids. The method is based on the introduction of a volume fraction function for each phase. The function is constant inside a selected phase and exhibits sharp changes at the interface between phases. A multiphase system can thus be treated as a single medium with sharply changing parameters at the interfaces. The physical properties of this phase are calculated in any point by the values of the volume fractions. The Navier-Stokes equations describing the system can be solved over the entire computational domain. The VoF method is implemented in ANSYS FLUENT used for modeling the pattern formation.

The influence of vibrations is taken into account by introducing a periodically varying volumetric force. Temporal discretization is performed by the first-order scheme. Note that the time step has to be much smaller than the period of vibrations while the frequency of vibrations is quite high. The computational error of the first-order scheme is therefore small. The spatial discretization is performed using the third-order MUSCL scheme (monotone upstream-centered schemes for conservation laws).

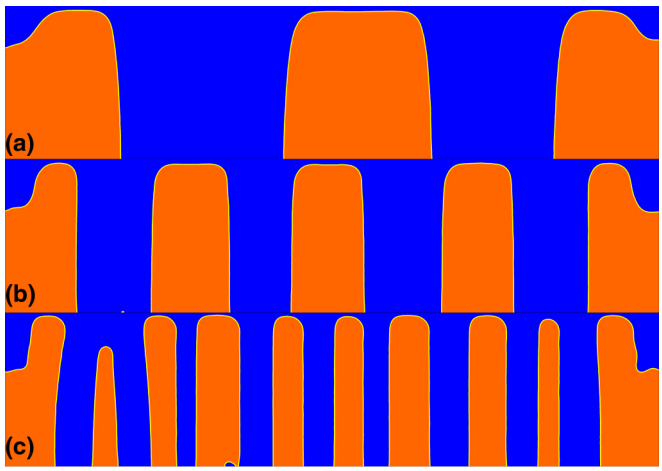

FIG. 4. Quasistationary band patterns in a two-layer system of silicon oil and Galden HT135 with densities and viscosities corresponding to experiment [18] (see text). Vibration characteristics are $f = 30$ Hz: (a) $a = 1.0$ mm; (b) $a = 1.6$ mm; (c) $a = 2.6$ mm.

Figure 4 presents the quasistationary band patterns calculated for the two-layer system of immiscible liquids used in the experiments [18] performed under the earth gravity field. The fluids are silicon oil (dynamic viscosity $\eta_2 = 0.202$ Pa s and density $\rho_2 = 962\,\mathrm{kg/m^3}$) and Galden HT135 (dynamic viscosity $\eta_1 = 1.96 \times 10^{-3}$ Pa s and density $\rho_1 = 1752\,\mathrm{kg/m^3}$). A surface tension of $\alpha = 6.8 \times 10^{-3}$ N/m was reported in [8]. The fluids occupy equal volumes of a container of length $L = 8.5$ cm and height $h = 2$ cm. The vibration frequency is $f = 30$ Hz and the amplitude is varied. As one can see, the wavelength of the band pattern decreases when the vibration amplitude increases. (In Sec. IV a quantitative comparison is made among the direct numerical simulation results, the analytical formula Eq. (27) for inviscid fluids, and the linear stability results for viscous fluids.)

To analyze the viscosity effect on the band pattern formation we carried out calculations by considering a system of fluids having the same parameters as in [18] except for viscosities whose values were varied. The simplest case, when the dynamic viscosities of both fluids are equal, $\eta = \eta_1 = \eta_2$, was studied. Figure 5 shows the patterns calculated for the vibration amplitude $a = 1.8$ mm. As one can see, the pattern wavelength grows with η. The dependence of the pattern wavelength on viscosity η is plotted in Fig. 6.

Taking into account that for the liquid-vapor system, the surface tension tends to zero when approaching the critical point, we also performed the calculations for the case of zero surface tension and varying the fluid viscosity (Fig. 7). As in the case of nonzero surface tension, the band pattern formation is observed and the band pattern wavelength grows with the increase of η . The differences from the case of nonzero surface tension can be seen in the disruption of the domains near the

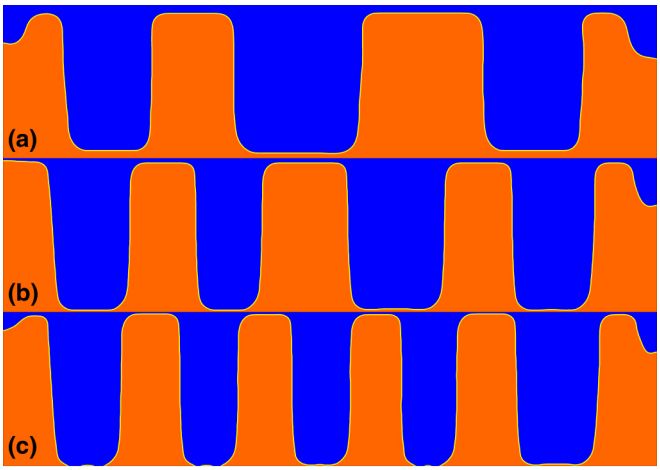

FIG. 5. Evolution of quasistationary band patterns with the decrease of dynamic viscosity for the vibration characteristics $f = 30$ Hz and $a = 1.8$ mm. Dynamic viscosities of both fluids are made equal (see text): (a) $\eta = 0.2$ Pa s; (b) $\eta = 0.075$ Pa s; (c) $\eta = 0.04$ Pa s.

boundaries. Similar patterns were observed in experiments with miscible fluids in [19].

IV. COMPARISON OF DIRECT NUMERICAL SIMULATIONS WITH LINEAR STABILITY ANALYSIS

We now compare the results of direct numerical simulations (Sec. III above) and of numerical solutions of the linearized problem of evolution of small perturbations (Sec. II D above). Figure 8 shows the variation of the dimensionless vibrational parameter B as a function of the dimensionless wave number of

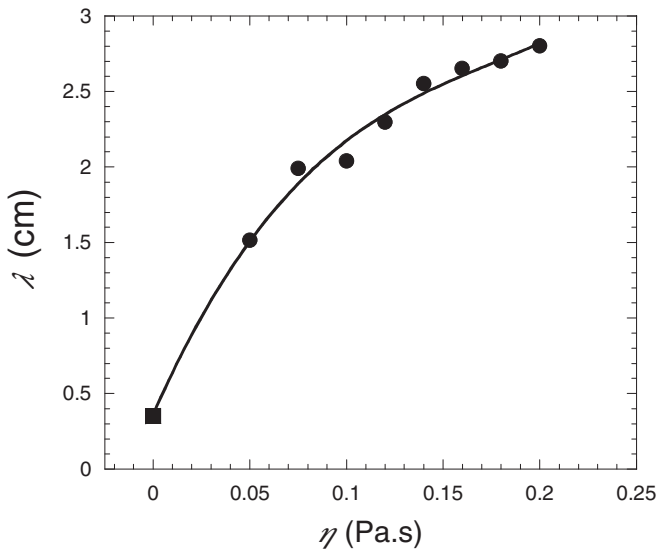

FIG. 6. Dependence of the pattern wavelength λ^* (cm) on dynamic viscosity η (Pa s) for vibration characteristics $f = 30$ Hz and $a = 1.8$ mm. Filled circles are the results of DNS (see Fig. 5); the solid curve is a smoothing function. The full square is the value calculated from the analytical formula Eq. (28) obtained for inviscid fluids.

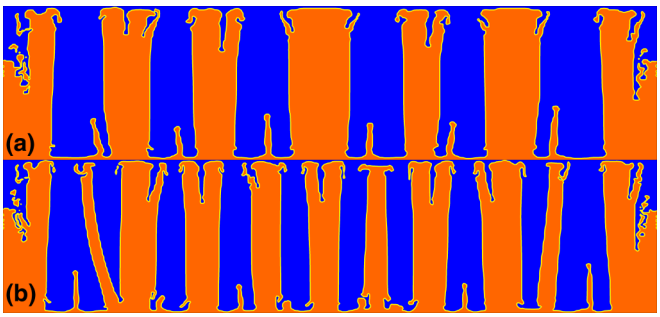

FIG. 7. Evolution of quasistationary band patterns calculated for zero surface tension with the decrease of dynamic viscosity (same for both fluids) (a) $\eta = 0.075$ Pa s, (b) $\eta = 0.05$ Pa s. Vibration characteristics are $f = 30$ Hz, $a = 1.8$ mm.

the band patterns obtained by direct numerical simulation (see Fig. 4), by the solution of the linearized problem (34)–(36) and from the analytical formula (27) obtained for inviscid fluids, for two different two-layer systems. As one can see from Fig. 8(a) (silicon oil and Galden HT135), the agreement between the linear stability results for viscous fluids and the direct numerical simulation is quite good, while the analytical solution for inviscid fluids gives the correct prediction only for small B. All three approaches give the dependence $B(k)$ close to linear in the considered range of B.

We also performed the comparison of direct numerical simulations and solution of linear stability problem for viscosities and surface tension values closer to the experiments performed with CO_2 on board the sounding rockets [see Fig. 8(b)].

The following parameter values were considered: the total thickness of the layers $h = 2$ cm; densities of lower and upper fluids 2000 and 1000 kg/m^3, respectively; surface tension 2.5×10^{-7} N/m; vibration frequency 30 Hz; and vibration amplitude was varied. Dynamic viscosities of both fluids were taken to be equal to 0.026 Pa s. This value is still substantially higher than that for CO_2; however, DNS cannot be performed for very low viscosities of fluids used in the experiments because of very thin dynamic boundary layers.

The calculations show that in this parameter range the agreement between both approaches is also quite good. As one can see from Fig. 8(b), in this parameter range the dependence of B on the dimensionless wave number of the band pattern, k, is substantially nonlinear.

V. EXPERIMENTAL RESULTS WITH CO_2 AND H_2

Experiments have been performed with CO_2 on board the sounding rockets MiniTexus5 (initial spinning, 180-s free fall) [10], Maxus5 (no spinning, 780-s free fall) and Maxus 7 (no spinning, 780-s free fall) [11]. In sounding rockets the residual level of gravity is very low, down to $10^{-5}g$, with very low g-jitter [20]. The cell body is made of a block of copper-cobalt-beryllium alloy in which are drilled one cylinder (Maxus7) or three (MiniTexus5, Maxus5) with inner diameter about 10 mm diameter. Two sapphire windows (9 mm thickness) are epoxied at each cylinder ends at distance e varying between 2 and 10 mm. Three successive modules (the first two modules were unfortunately damaged due to recovery problems in

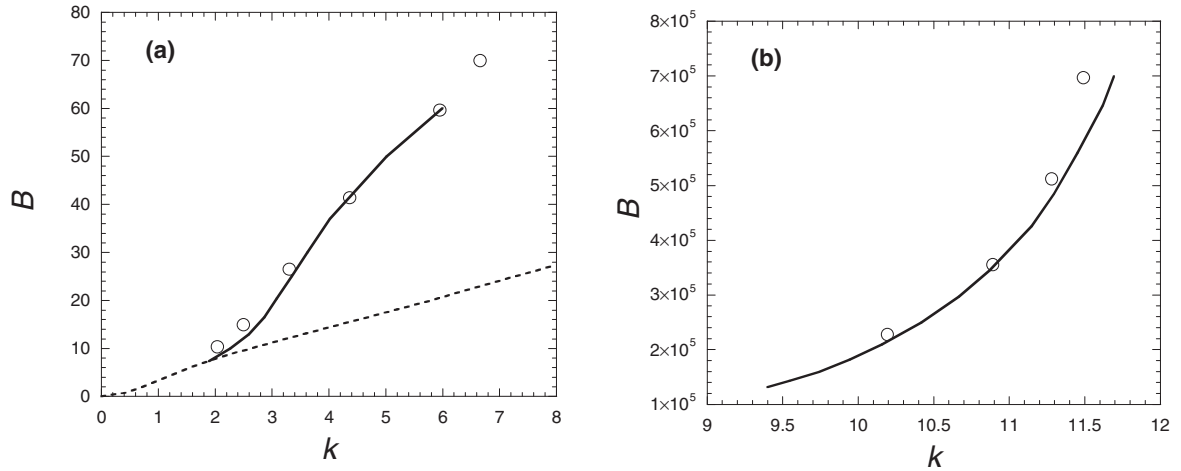

FIG. 8. Variation of the dimensionless vibrational parameter B with the dimensionless wave number k of the band pattern. Solid curve: From the numerical solution of the linearized problem of small perturbation evolution for viscous fluids [Eqs. (34)–(36)]. Circles: From direct numerical simulation. The interrupted curve is the inviscid solution Eq. (27). (a) Silicon oil and Galden HT135; (b) small surface tension and viscosity (near critical CO_2 [10–12], see text).

MiniTexus5 and Maxus5) are of TEM-FER type [9–11]. Using CuCoBe alloy ensures good thermal conduction between the fluid and the thermostat. The latter is an Al cylinder in which is inserted the CuCoBe block. It is thermally regulated by a Peltier element within 0.3 mK accuracy. Temperature can be adjusted within 1-mK steps. As the module has to work under vacuum during the flight, the thermostat remains pressurized at 1 bar pressure.

The cylinder is hosted in one of a two-arms symmetric shaker vibrating device. In order to prevent vibrations of the rocket, another block (hosting experiments with vibrated granular materials [21]) with the same mass is vibrated in the opposite arm, in phase opposition. The couple of the motor is also compensated to prevent rocket rotation. The shaker can apply linear harmonic vibrations in a range of amplitude $a = [0.1–2.5]$mm and frequency $f = [0.5–60]$Hz; a and f can be varied independently step by step.

The critical point data of CO_2 are listed in Table I. The critical temperature ($T_c = 304.13$ K) was determined within 0.5 mK (not in an absolute temperature scale), which is the limiting precision that can be achieved on ground due to the gravity-induced hydrostatic gradients. The fluid is indeed compressed under its own weight over its 10-mm height. In addition, the smallest temperature step available is of 1 mK amplitude.

The sequence of temperature and vibration amplitude and frequency events are either teleoperated from the ground (MiniTexus5 and Maxus5) or initially programmed with possibility of remote control (Maxus7). Video images are telemetered to the ground (MiniTexus5 and Maxus5) or recorded on board (Maxus7). Onboard recordings ensure better quality pictures [see Figs. 1(a)-(c) and 9]. The experiment parameters, especially cell temperature, vibration amplitude, and frequency, are telemetered.

A. CO_2 in MiniTexus5 and Maxus 5

The three cells (diameter $2R = 10.8$ mm and thickness $e = 10.8$ mm) are filled with CO_2 at different densities. The same cells, labeled 1, 2, and 3 are used on board MiniTexus5 and Maxus5. The filling density ratios $\delta\rho^* = (\rho_v - \rho_c)/\rho_c$ are listed in Table II. Uncertainties are $\pm 1 \times 10^{-3}$. They are determined with the variations of meniscus height on the ground at different temperatures below T_c [22]. The corresponding coexistence temperatures, T_{cx}, where fluid phase separates into gas and liquid phase, are deduced from the asymptotic coexistence amplitude variation,

$$\Delta\rho^* = \frac{\rho_v - \rho_c}{\rho_c} = B'\left(\frac{T_c - T_0}{T_c}\right)^{\beta}, \tag{37}$$

with the universal critical exponent $\beta = 0.325$ and critical amplitude B' (see Table I). The values of T_c–T_{cx} are listed in Table II. The vapor volume fraction of cells 1 and 2 depends on temperature, whereas it is always 50% for cell 3 at critical density. The temperature value at which the sample phase separates varies with even minute impurities. The values are listed in Table II. Cells 1 and 3 have nearly the same T_c whereas cell 2 presents a depletion of 12 mK with respect to 1 and 3. As all three samples are at the same temperature, they can thus appear in different, one- or two-phase states.

S-VHS video recording and image digitization are used to determine the characteristics of the interface. A photodiode continuously illuminates the interfaces by light transmission through the cell for vibration frequencies smaller than 30 Hz.

TABLE I. Fluid parameters (from [6]).

Fluid	T_c(K)	p_c(MPa)	ρ_c(kg m^{-3})	B'	α_0(10^{-2} N m^{-1})	η(10^{-5} Pa s)
CO_2	304.14	7.375	467.8	1.60	6.72	4.21
$n - H_2$	33.19	1.315	30.11	1.61	0.542	0.27

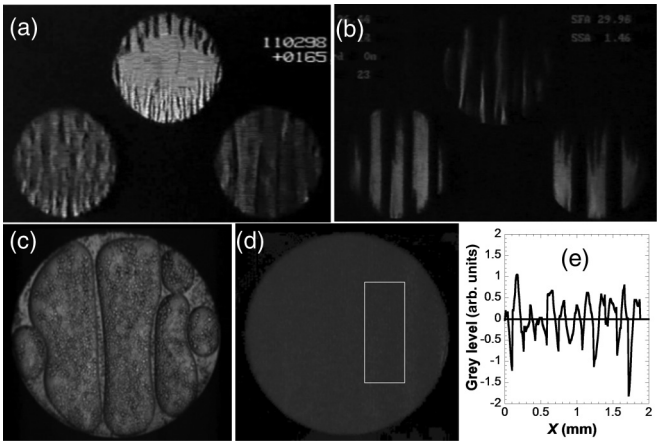

FIG. 9. Images of CO_2 vibrated cells. (a) MiniTexus5 $a = 0.1$ mm, $f = 60$ Hz, T–$T_c(1, \text{left}) = -15.06$ mK; T–$T_c(+2, \text{middle}) = -1.4$ mK; T–$T_c(3,\text{right}) = -15.2$ mK. The central cell is above T_c and then homogeneous but the density difference in the thermal boundary layer induces a fingering vibrational Rayleigh instability on the horizontal walls (see [22] and references therein). (b) Maxus5 $a = 1.5$ mm, $f = 30$ Hz, T–$T_c(3, \text{left}) = -20$ mK; T–$T_c(2,\text{middle}) = -6.2$ mK; T–$T_c(1,\text{right}) = -19.9$ mK. (c,d) Maxus 7 (see also Fig. 1) T–$T_c = -2.4$ mK: (c) $a = 0.2$ mm, $f = 5.57$ Hz; (d) $a = 2.5$ mm, $f = 19.8$ Hz corresponding to the smallest band pattern wavelength. (e) Analysis of window drawn in (d): Gray level variation along horizontal space ordinate X parallel to vibration direction showing band periodicity.

For higher vibration frequencies the cell is illuminated by a stroboscope with a flash duration of 1 ms. The final spatial resolution is of the order of 30 μm.

In MiniTexus5 experiments, the 180-s free fall timeline is separated in an initial 20-s relaxation of fluid motion after rocket despinning, and 20-s observation for different sets of $(a,\ f)$ vibration parameters (Table II). Temperature is maintained constant at the level T_0 before lift-off during nearly the entire mission duration (except near the end, at $t = 240$ s, temperature was increased at a constant $(a,\ f)$ by 31.45 mK above all sample T_{cx}'s). Temperature T_0 corresponds to different T–T_c and volume fraction values (see Table II), ranging from 23.7% to 50%. Volume fraction ϕ is calculated from the level rule:

$$\phi = \frac{\rho_L - \rho_0}{\rho_L - \rho_V} = \frac{1}{2} - \frac{\delta\rho^*}{2\Delta\rho^*}. \tag{38}$$

The Maxus5 experiment (Table II) was performed with the same cells and setup as in MiniTexus5. Vibration is applied after $t = 95$ s after lift-off, after more than 20-s relaxation time under weightlessness. The temperature timeline is the following. Temperature is firstly maintained constant during countdown and lift-off at temperature $T_0' = T_c(3) + 1.6$ mK where cells 1, 2, and 3 are all homogeneous. At $t = 120$ s, the temperature is quenched down by 5 mK to $T_1 = T_c(3) - 1$ mK. Cell 2 is at T_1–$T_{cx} = 13$ mK and cell 3 at T_1–$T_{cx} \approx 0$. Only cell 3 phase separates with 50% volume fraction. At $t = 385$ s, temperature is again decreased by 15 mK to $T_2 = T_c(3) - 16$ mK, where both cells 1 and 2 phase separate with near-equal volume fractions, 30.6% (1) and 27.3% (2). Cell 3 also phase separates but remains at 50% volume fraction.

TABLE II. Characteristics of the cells and timeline for the weightlessness experiments with CO_2. Left, middle, and right cells correspond to their position in Fig. 9. (Notations: see text).

Cell	MET time (s after lift-off)	Cell 1	Cell 2	Cell 3
$\delta\rho^*(\%)(i = 1,2,3)$		2.53	1.56	0
T_c–T_{cx}(mK)		0.86	0.19	0
T_{cx}–$T_{cx}(3)$(mK)		−1	−14	0
MiniTexus5	*Start 0g: 90 End 0g: 260*	Left L	Middle M	Right R
T_0–T_{cx}(mK)	–1200–260	−14.2	−1.2	−15.2
$T_0 - T_c$(mK)		−15.06	−1.4	−15.2
ϕ (%)		30.3	23.7	50
Maxus5	*Start 0g: 75 End 0g: 840*	Right R	Middle M	Left L
T_0'–T_{cx} (mK)	–1200–120	5	18	4
$T_0' - T_c$ (mK)		4.14	17.81	4
T_1–T_{cx}(mK)	120–385	0	13	−1
T_1–T_c(mK)		−0.86	9.81	−1
ϕ (%)				50
T_2–T_{cx}(mK)	385–510	−15	−2	−16
T_2–T_c(mK)		−15.86	−2.19	−16
ϕ (%)		30.6	27.3	50
T_3–T_{cx}(mK)	510–840	−19	−6	−20
T_3–T_c(mK)		−19.86	−6.19	−20
ϕ (%)		32.0	33.8	50
Maxus7	*Start 0g: 75 End 0g: 840*			
T_0–T_c	–1200–150			2
T_1–T_c	150–385			−2.4
ϕ (%)				50

All three samples are then in the two-phase region. Later, at $t = 510$ s, temperature is further decreased by 4 mK to $T_3 = T_c(3) - 20$ mK. All three cells again phase separate, with volume fractions 32%, 33.8%, and 50%.

B. CO_2 in Maxus 7

Only one cell is concerned, with the body made of a CuCoBe alloy. The fluid is confined in an inner cylindrical volume, with radius $R = 5.0$ mm and $e = 2.189$ mm thickness, closed at each end by two parallel sapphire windows. The sample is illuminated by parallel light issued from a LED and observed in transmission by the cameras. Coherent illumination is used to enhance the refractive-index gradients and then the density gradients. The cell is filled at critical density with a precision of 0.1%, by checking the temperature variation of the meniscus position according to the method developed in [23].

Although the vibration module is basically the same as previously used in MiniTexus5 and Maxus5 experiments, the optics is improved. Images are taken by a high-resolution, 2048 × 2048 pixels, 5 fps frame rate, 125 μs full-frame shutter times, fixed gain, digital camera (type TM4100 from Pulnix). It is equipped with a long-working-distance microscope. Images are stored on the rocket module and recovered after the flight. With an imaging factor from object to chip of 1:1.12 typically, the final spatial resolution is of the order of 1 pixel (7.4 μm × 7.4 μm). Image analysis is then used to determine the characteristics of the pattern. All other scientific data, including images with low resolution (782 × 582 pixels) from a 25 Hz CCD camera (type XC 8500 from Sony), temperature measurements (PT 100 sensors), vibration amplitude and frequency, and acceleration data, are sent by telemetry to the ground.

The timeline (Table II) is the following. Equilibration is ensured until $t = 75$ s, 2 mK above T_c. Then vibration is applied. A temperature quench of 4.4 mK is performed at $t = 150$ s. The cell is maintained at the same temperature until the end of the period allocated for the experiment ($t = 385$ s). Typical patterns from the three sounding rockets experiments are reported in Fig. 9 as a complement of Fig. 1.

C. H_2 under magnetic levitation

Experiments with H_2 are performed in the cryogenic facility HYLDE (hydrogen levitation device [24,25]). The HYLDE setup uses a 10-T magnetic field generated by a cylindrical superconducting coil. Hydrogen can be levitated near the upper end of the coil where there is a near-constant magnetogravitational potential field. Quettier *et al.* [26] have shown that the technique of magnetic levitation using a solenoid of cylindrical configuration can give total compensation of gravity only at a single point. A residual gravity field is radially directed towards the center of the cell. The uniformity of the gravity field depends on the size of the cell. Using the setup HYLDE a uniformity better than 1% and 2.5% can be achieved in cells of side $h = 3$ mm.

As the setup has been described in detail in several publications—see, e.g., [24,25]—we only report its main features. A superconducting coil made of Nb-Ti is dipped inside liquid helium at a temperature of 2.16 K and a pressure

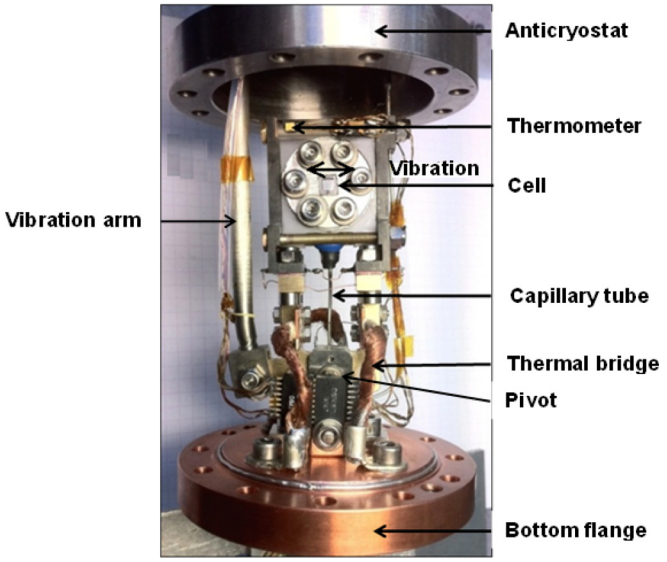

FIG. 10. Experimental cell of size 3mm × 3mm × 2mm.

of 0.1 MPa inside a cryostat. The experimental cell is mounted inside another cryostat (called "anticryostat") maintained under a vacuum of less than 10^{-7} mbar. Endoscopes for a light source and a video camera are mounted inside the anticryostat. The positions of the endoscopes are independently adjustable.

The experimental cell used (Fig. 10) is a cubical cavity of size 3 mm × 3 mm × 2 mm with H_2 initially at room temperature. The fluid is thus n–H_2, whose critical point data are listed in Table I. Hydrogen is filled inside the cell using a capillary tube of inner diameter 0.5 mm. To determine the critical density, the cell is filled up to half its height at a temperature very close to the critical point (say 50 mK) and the meniscus is monitored for small temperature increase or decrease of the cell (50 mK on either side of the filling temperature). If the level of the meniscus does not change with temperature, it means that the cell is filled at its critical density. This method of filling the cell at the critical density of the fluid is quite precise and is close to 0.2% of the critical density ρ_c. The capillary tube is fitted with a thermal switch, made of a small block of copper continuously cooled under the triple point of H_2 by a copper wire connected to the helium bath. It is heated whenever required using a resistive heater. In the absence of heating, hydrogen inside the capillary tube freezes, thus closing the cell. The experimental cell is provided with thermal bridges, strands of copper wires connecting the bottom flange of the anticryostat—which is maintained at liquid helium temperature—and the cell. Resistive heaters in thermal contact with the cell are used to heat and control the temperature of the cell. Two thermometers are pasted on either side of the cell to monitor the temperature of the cell. The temperature control of the cell is achieved by using a standard Proportional-Integral-Derivative (PID) control system.

The cell is oscillated along a pivot (Fig. 10) with various frequencies ($f = 10$–50 Hz) and various amplitudes ($a = 0.1$–1 mm). It is estimated that for a frequency of 50 Hz and for a maximum amplitude of 1 mm, the cell experiences an oscillation in the vertical direction of ±10 μm, which is negligible compared to the amplitude of the horizontal

vibration. Also, the resulting centripetal acceleration compares to the vibrational acceleration as a/R (where a is the amplitude of vibration and R is the distance of the cell from the pivot), which comes out to be of the order of 1/60. Thus the centrifugal force is negligibly small in the experimented frequency and amplitude ranges and the vibration can be assumed to be in the horizontal direction.

Typical patterns are reported in Figs. 1(d) and 1(e). Note that, since the thermometers fixed to the cell vibrate along with the cell inside an intense magnetic field, eddy currents are induced inside them and their electric cabling provoking unwanted oscillations in the temperature electric signal. This renders the values of the temperature during the vibration experiments useless. However, temperature can be estimated as explained in [9] with the measure of the thickness of the bubble interface, t_m, under residual gravity $g^* \approx 0.01g$. This thickness is proportional to the capillary length $l_c = (\alpha/g^*\delta\rho^*)^{1/2}$ and the liquid-vapor refractive index difference, itself proportional to $\Delta\rho^*$: $t_m \sim \Delta\rho^* l_c \sim (T_c\text{–}T)^{\nu+\beta/2=0.79}$ from Eqs. (37) and (40). This method is relatively precise; see the discussion in [9].

D. Comparison with theory and simulation

The number p of bands in each image gives the wavelength $\lambda^* = 2R/p$ and the nondimensional wave vector:

$$k = \frac{2\pi R}{\lambda} = \pi p. \tag{39}$$

The number of bands was counted manually when it was easy to do it (high contrast, small band number). For more difficult cases, image analysis software was used. An example is given in Figs. 9(d) and 9(e) corresponding to the image and analysis of the smallest band pattern wavelength. Note that the bands showing Faraday instability have been counted as well. Faraday instability is indeed localized at the liquid-vapor interface only after the band pattern has formed. The value of the vibration parameter B can be calculated from Eq. (22) where $h = R(= 5.0\,\text{mm})$ for CO_2 and $h = e/2(= 1.5\,\text{mm})$ for H_2. The density difference is calculated from Eq. (37). The liquid-vapor surface tension is deduced from the power law dependence [6,7,8]:

$$\alpha = \alpha_0 \left(\frac{T_c - T}{T_c}\right)^{2\nu}. \tag{40}$$

Here $\nu = 0.63$ is the critical exponent. One thus obtains

$$B = B_0(a\omega)^2(T_c - T)^{\beta-2\nu=-0.935}. \tag{41}$$

The parameter $B_0 = 5.84 \times 10^3\,\text{m}^{-2}\,\text{s}^2$ for CO_2 and $B_0 = 1.77\,\text{m}^{-2}\,\text{s}^2$ for H_2 by using the values of Table I. Note that experiments with CO_2 in sounding rockets and H_2 under magnetic levitation are complementary. With CO_2 the vibration parameters (a, ω) are changed at a few rigorously constant temperatures, making a precise determination of $B(k)$, but the $B(T)$ variation cannot be precisely determined as only a few temperatures are available. In contrast, in H_2 experiments, temperature variation at constant (a, ω) is continuous, giving more accurate $B(T)$ dependence. However, $B(k)$ at constant temperature, obtained indirectly, is less reliable.

In Fig. 11 are presented the results of space experiments Maxus 7, Maxus 5, and MiniTexus 5. The two-phase system used in the experiments (CO_2 liquid-vapor phases) is characterized by low viscosities and very small interfacial tension. It made it impossible to carry out a direct simulation for such experimental parameters because too fine mesh is needed. However, one can perform the numerical solution of the linearized problem (which is one dimensional). The calculations were thus performed with the same dimensionless kinematic viscosities for both phases ($\nu_1 = \nu_2 \approx 5 \times 10^{-5}$) corresponding to typical experimental values (density ratio $\rho = 1.07$, Weber number $\text{We} = 1 \times 10^7$) and various dimensionless vibration amplitude A. The results show good agreement in spite of the scatter of experimental data.

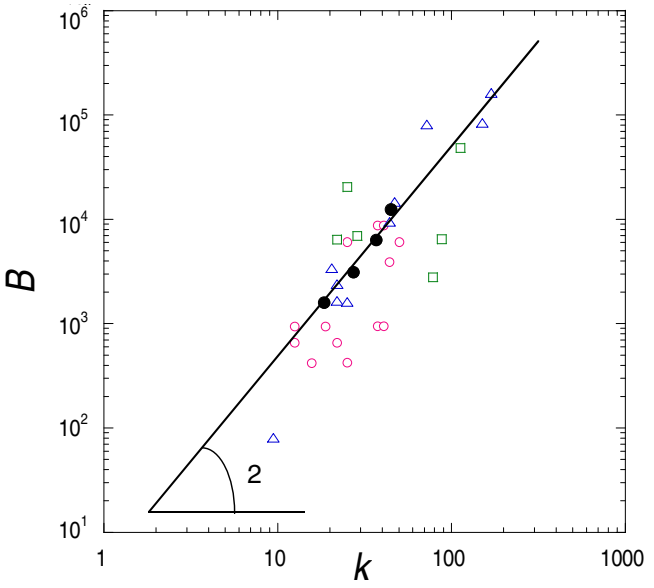

FIG. 11. Comparison of space data from Maxus 7 (triangles), Maxus 5 (open squares), and MiniTexus 5 (open circles) with the results of the linear stability analysis for viscous fluids [full circles, $(\nu_1 = \nu_2 \approx 5 \times 10^{-5})$] which can be approximated by a power law with exponent 2.

Note that the data approximatively follow a power law $B \sim k^2$. It is thus possible to extract the k temperature dependence at constant $a\omega$. From Eq. (41), and the assumption $B(k) \sim k^2$ one gets

$$k \sim (T\text{–}T_c)^{-0.5}. \tag{42}$$

In Fig. 12 is reported the temperature dependence of k for H_2. The data approximatively follow a power law with exponent -0.7 ± 0.14 (two standard deviations). This value is somewhat larger than the expected value of -0.5 [Eq. (42)]. At least two reasons can be put forward to explain the difference. First, Eq. (42) is empirical. Second, the temperature determination in the experiments is only indirect and uncontrolled bias can occur, especially for the data the furthest from the critical temperature where the interfacial thickness is large. As a matter of fact, the data the closest to T_c fit the power law Eq. (42).

VI. CONCLUDING REMARKS

This study addresses the questioning phenomenon of periodical patterns developing under zero-gravity conditions at the

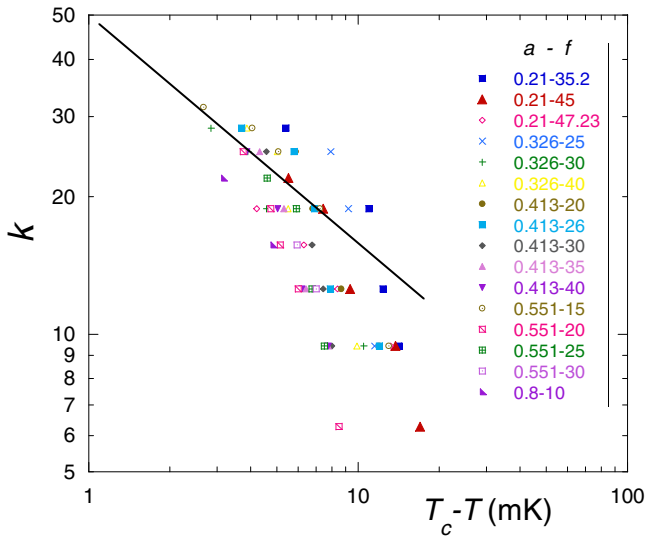

FIG. 12. Variation of the pattern reduced wave number k with respect to temperature T_c–T. Vibration parameters $(a,\ f)$ are indicated in the figure. Full line: Power law with exponent -0.5 [Eq. (38)].

interface of two immiscible fluids under vibrations parallel to interface. The fluids (CO_2, H_2) are close to their critical point, with low viscosity, low surface tension, and small difference in liquid-vapor densities. The patterns have been identified by some of us when experiments under vibration were performed under weightlessness; a systematic study is here reported. Although the phenomenon is reminiscent of frozen wave instability observed under a gravity field, the present theoretical analysis and numerical simulations show they are not identical. In particular, no threshold is found in the band instability, in contrast to the frozen wave case under gravity field. The neutral curve does not present any minimum and the selection of the critical wavelength arises. Results of the present linear stability analysis, direct numerical simulation, and experimental observations corroborate the hypothesis that the wavelength selection is based on the perturbation growth rate: The pattern wavelength in experiments corresponds to the wavelength of the perturbations with maximal growth rate. Note that this wavelength differs substantially from the neutral perturbations wavelength at the same vibrational parameter value. The role of viscosity is highlighted in the pattern formation, with a critical wavelength dependence on vibration parameters that strongly depends on viscosity.

ACKNOWLEDGMENTS

D.B., G.G., Y.G., and C.L. acknowledge partial funding support by Centre National d'Etudes Spatiales (CNES). They also thank the European Space Agency (ESA) for its support in sounding rocket experiments. The theoretical analysis and numerical calculations were carried out in the framework of preparation of space experiment VIPIL on board the ISS. They were supported by Roscosmos, Perm Region Government (Grant No. C-26/004.03) and Russian Foundation for Basic Research (Grant No. 15-01-09069).

[1] M. Faraday, Philos. Trans. R. Soc. London **121**, 299 (1831).
[2] K. Kumar and L. S. Tuckerman, J. Fluid Mech. **279**, 49 (1994).
[3] G. H. Wolf, Z. Phys. B **227**, 291 (1969).
[4] D. V. Lyubimov and A. A. Cherepanov, Fluid Dyn. **21**, 849 (1987).
[5] R. Wunenburger, P. Evesque, C. Chabot, Y. Garrabos, S. Fauve, and D. Beysens, Phys. Rev. E **59**, 5440 (1999).
[6] B. Zappoli, D. Beysens, and Y. Garrabos, *Supercritical Fluid Hydrodynamics* (Springer, New York, 2015).
[7] H. E. Stanley, *Introduction to Phase Transitions and Critical Point Phenomena* (Oxford University Press, Oxford, 1971).
[8] A. Onuki, *Phase Transition Dynamics* (Cambridge University Press, Cambridge, 2002).
[9] G. Gandikota, D. Chatain, S. Amiroudine, T. Lyubimova, and D. Beysens, Phys. Rev. E **89**, 013022 (2014).
[10] D. Beysens, R. Wunenburger, C. Chabot, and Y. Garrabos, Micrograv. Sci. Technol. **11**, 113 (1998).
[11] D. Beysens, D. Chatain, Y. Garrabos, C. Lecoutre, F. Palencia, P. Evesque, and V. Nikolayev, Acta Astron. **61**, 1002 (2007).
[12] D. Beysens, Y. Garrabos, D. Chatain, and P. Evesque, Europhys. Lett. **86**, 16003 (2009).
[13] V. S. Nikolayev, D. Chatain, D. Beysens, and G. Pichavant, Microgravity Sci. Technol. **23**, 113 (2011).
[14] G. Gandikota, D. Chatain, S. Amiroudine, T. Lyubimova, and D. Beysens, Phys. Rev. E **89**, 012309 (2014).
[15] S. Fauve, K. Kumar, C. Laroche, D. Beysens, and Y. Garrabos, Phys. Rev. Lett. **68**, 3160 (1992).
[16] D. V. Lyubimov and T. P. Lyubimova, Model. Mech. **4**, 136 (1990) (in Russian).
[17] A. V. Burnysheva, D. V. Lyubimov, and T. P. Lyubimova, Fluid Dyn. **46**, 1000 (2011).
[18] S. V. Jalikop and A. Juel, J. Fluid Mech. **640**, 131 (2009).
[19] Y. Gaponenko, M. M. Torregrosa, V. Yasnou, A. Mialdun, and V. Shevtsova, Soft Matter **11**, 8221 (2015).
[20] H. U. Walter, *Fluid Sciences and Materials Science in Space: A European Perspective* (Springer-Verlag, Berlin, 2012).
[21] E. Falcon, R. Wunenburger, P. Evesque, S. Fauve, C. Chabot, Y. Garrabos, and D. Beysens, Phys. Rev. Lett. **83**, 440 (1999).
[22] G. Gandikota, S. Amiroudine, D. Chatain, T. Lyubimova, and D. Beysens, Phys. Fluids **25**, 064103 (2013).
[23] C. Morteau, M. Salzmann, Y. Garrabos, and D. Beysens, in *Proceedings of the Second European Symposium "Fluids in Space", Naples, Italy, 22–26 April 1996*, edited by A. Viviani (Edizioni Jean Gilder Congressi srl, Naples, 1996), pp. 327–333.
[24] R. Wunenburger, D. Chatain, Y. Garrabos, and D. Beysens, Phys. Rev. E **62**, 469 (2000).
[25] D. Chatain, D. Beysens, K. Madet, V. Nikolayev, and A. Mailfert, Microgravity Sci. Technol. **18**, 196 (2006).
[26] L. Quettier, H. Félice, A. Mailfert, D. Chatain, and D. Beysens, Eur. Phys. J.: Appl. Phys. **32**, 167 (2005).